J. Phys. Chem. A 2009, 113, 5657–5670 5657

DFT/TDDFT Exploration of the Potential Energy Surfaces of the Ground State and Excited States of $Fe_2(S_2C_3H_6)(CO)_6$: A Simple Functional Model of the [FeFe] Hydrogenase Active Site

Luca Bertini,* Claudio Greco, Luca De Gioia, and Piercarlo Fantucci*

Department of Biotechnology and Biosciences, Universitá degli Studi di Milano—Bicocca,
Piazza della Scienza 2, 20126 Milan, Italy

Received: October 22, 2008; Revised Manuscript Received: March 12, 2009

$Fe_2(S_2C_3H_6)(CO)_6$ (**a**) is a simple model of the [FeFe] hydrogenase catalytic site. The topology of the potential energy surface (PES) of this complex, of its cationic and anionic species ($\mathbf{a}^+$ and $\mathbf{a}^-$), and of its lowest triplet state was studied using density functional theory (DFT) with BP86 and B3LYP functionals, while selected low- and high-lying singlet excited states were studied with the time-dependent density functional theory (TDDFT). The global minima of **a** and $\mathbf{a}^-$ PESs are characterized by an all-terminal CO ligand arrangement, while the two rotated forms are transition states (TS). On the contrary, for the $\mathbf{a}^+$ and lowest triplet state PES, the three forms considered are local minima, and the syn rotated form is the global minimum. The relative stability of the rotated forms and the all-terminal CO form on the **a**, $\mathbf{a}^+$, and $\mathbf{a}^-$ PESs is discussed in light of the Quantum Theory of Atoms in Molecules (QTAIM) analysis of the electron density. By comparing the Fe−Fe bond features of the three forms for each PES, we found that the global minimum structure is characterized by the shortest Fe−Fe bond distance and highest electron density at the Fe−Fe critical point. This approach gave evidence that in the **a** rotated forms, the weak $Fe-C_\mu$ interaction between the Fe atom of the unrotated $Fe(CO)_3$ and the C atom of the semibridged CO is formed to the detriment of the Fe−Fe bond interaction. These results suggest that the stabilization of the rotated forms on the cationic PES might be due to the formation of the weak $Fe-C_\mu$ interaction minimizing the weakening of the Fe−Fe bond. The low-lying and lowest triplet excited-state PES investigated are characterized by the stabilization of the rotated forms over the all-terminal CO ligand arrangement. On the first singlet $1^1A''$ excited-state PES, an $Fe(CO)_3$ semirotated structure is the lowest-energy stationary point, while the exploration of the $1^1A'$ and $2^1A''$ singlet excited PESs evidences the stabilization of the rotated over the all-terminal CO forms. Singlet excited-state optimized geometry results are compared with excited-state nuclear distortions recently obtained from resonance Raman excitation profiles. Finally, the results of the exploration of the $6^1A'$ and $9^1A'$ high-lying excited PESs are discussed in light of the recent ultraviolet photolysis experiments on **a**.

1. Introduction

[FeFe] hydrogenases catalyze the reduction of protons to molecular hydrogen in a wide variety of microorganisms. The active site named H-cluster[1] is composed of an $\{Fe_4S_4\}$ cubane subcluster bridged by a cysteine residue to an $\{Fe_2S_2\}$ binuclear cluster (Chart 1).

In the $\{Fe_2S_2\}$ subcluster, two COs and two CN^-'s are terminally coordinated ligands, and the two iron atoms are bridged by one CO and a bidentate $-SCH_2-X-CH_2S-$ ligand, where the chemical nature of the X group is still matter of debate ($-CH_2-$, $-NH-$, or $-O-$).[2] In the active form of the enzyme, the iron atom distal to the $\{Fe_4S_4\}$ subcluster has a vacant coordination site, which can be filled by external ligands. Three redox states of the $\{Fe_2S_2\}$ subcluster were characterized using spectroscopy techniques,[3−5] the fully reduced (Fe^IFe^I) form, the fully oxidized ($Fe^{II}Fe^{II}$) form, and a partially oxidized form that contains Fe^IFe^{II} metal centers. Mössbauer investigations gave evidence that the $\{Fe_4S_4\}$ subcluster remains in a global +2 oxidation state during the catalytic cycle.[6]

The possibility of clean and low-cost production of molecular hydrogen as an energy carrier prompted the synthesis of several biomimetic models of the [FeFe] hydrogenase catalytic site. One of the simplest models of the $\{Fe_2S_2\}$ subcluster is the $Fe_2(S_2C_3H_6)(CO)_6$ complex (**a** hereafter). This system is a member of the diiron hexacarbonyl complex family of general formula $Fe_2(\mu X_2)(CO)_6$, in which μX_2 denotes a dibridged ligand. In the present case, μX_2 is the 1-3-propanedithiolate $-SCH_2CH_2CH_2S-$ group (μ-pdt hereafter).

CHART 1: [FeFe] Hydrogenase Active Site

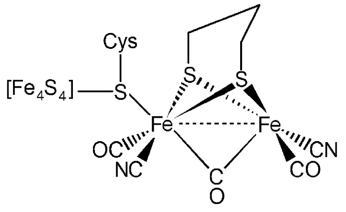

Complex **a** was synthesized in 1982,[7] and its structure was characterized by X-ray diffraction (XRD)[8] in 1999 and EXAFS in 2004.[9] This complex has an all-terminal ligand arrangement and is able to electrocatalyze proton reduction, although with a different mechanism compared with that of the enzyme.[10]

One of the most intriguing challenges in the design of biomimetic models of [FeFe] hydrogenases is to mimic the

---

* To whom correspondence should be addressed. E-mail: luca.bertini@unimib.it (L.B.); piercarlo.fantucci@unimib.it (P.F.).

10.1021/jp809347h CCC: $40.75

CHART 2: Schematic Drawings of the $Fe_2(S_2C_3H_6)(CO)_6$ All-Terminal CO (a) and the Two Rotated Structures (a_{syn} and a_{anti})

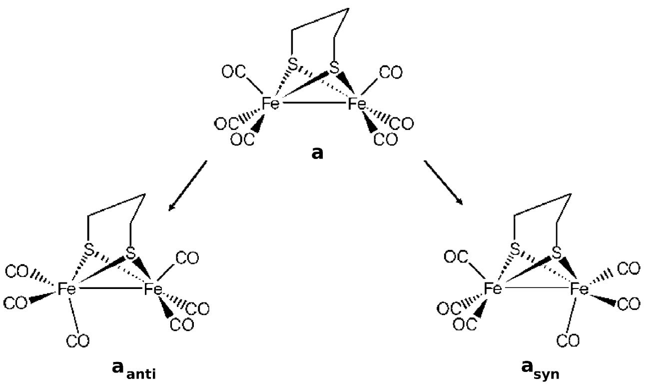

CHART 3: $Fe_2(S_2C_3H_6)(CO)_6$ Nomenclature of the CO Ligands Adopted in This Paper

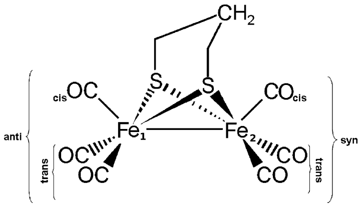

peculiar rotated ligand arrangement of the $\{Fe_2S_2\}$ cluster. In the case of the $Fe_2(S_2C_3H_6)(CO)_6$ complex, this ligand arrangement (**a**$_{syn}$ or **a**$_{anti}$) represents the transition state (TS) along the CO ligand cis–trans exchange path[11] and can be achieved by rotating the $Fe(CO)_3$ group around the Fe–Fe axis and moving one terminal CO ligand in the semibridged region (see Chart 2). In order to adhere as close as possible to the structural features of the [FeFe] hydrogenase catalytic site, a great effort has been devoted to the design of biomimetic models in which the rotated forms are stabilized with respect to the all-terminal CO form.

A possibility of stabilizing the rotated forms is to oxidize Fe^IFe^I models to the Fe^IFe^{II} redox state. For instance, the Fe^IFe^{II} cationic form of the complex (μ-pdt)$Fe_2(CO)_4(PMe_3)$(IMes) (IMes refers to 1,3-bis(2,4,6-trimethylphenyl)imidazol-2-ylidene)[12] resembles the structure of the Fe_2S_2 subcluster in the active oxidized form. Other examples are the Fe^IFe^{II} complexes proposed by Justice et al.[13,14] (($SCH_2CH_2S)Fe_2(CO)_3(PMe_3)$-(dppv)$BF_4$, dppv = *cis*-1,2-$C_2H_2(PPh_2)_2$) and by Felton et al.[15] (($SC_6H_4S)Fe_2(CO)_6^+$). Also, the $\{Fe_4S_4\}$ system proposed by Cheah et al.[16] ($(MeC(SCH_2)_3)_2Fe_4(CO)_8$) in its dianionic form has two COs in the bridging position.

Most of the experimental and theoretical studies on **a** were aimed at modeling the catalytic mechanism of dihydrogen cleavage, and usually, only the ground-state properties were considered. However, the photochemistry of the biomimetic models might be crucial in order to elucidate the mechanism of CO photolysis in the CO-inhibited [FeFe] catalytic site.[17] Recently, excited-state properties of **a** were investigated. Fiedler et al.[18] computed the **a** UV–vis spectrum using the time-dependent DFT technique, estimating the excited-state nuclear distortions from the analysis of the resonance Raman (rR) excitation profiles. The CO photolysis of **a** has been investigated by Ridley et al.[19] using ultrafast ultraviolet (UV) pump–IR probe spectroscopy at 330 nm. The authors gave evidence of the formation of two isomers of the metastable 16 electron complex (μ-pdt)$Fe_2(CO)_5$. Similarly, Brown-McDonald and coworkers[20] came to a similar conclusion by measuring IR spectra of the products obtained by irradiation of **a** with 365 nm light.

The aim of the present work is double. We provide a detailed analysis of the ground-state (**a** together with its cationic and anionic species) and selected excited-state (the first four low-lying and two high-lying singlet states and the lowest triplet state) PES topologies. Ground-state analysis results are used to discuss the factors affecting rotation of the $Fe(CO)_3$ groups, providing some general criteria for the synthesis of new and better biomimetic models. Finally, excited-state analysis results are discussed in light of the recent rR and CO photolysis experiment results.

2. Computational Details

Computations were performed using the pure gradient-generalized approximation (GGA) BP86[21,22] and hybrid B3LYP[23,24] DFT functionals. The resolution of identity (RI) technique[25] was adopted for BP86 computations. Basis sets of triple-ζ plus polarization split valence quality (TZVP hereafter)[26] were adopted for all atoms in the complexes, and the DFT grid size was set to the standard *m*3 value. Analytic gradients for the excited-state energy were computed using the EGRAD routine recently implemented[27] within the TURBOMOLE[28] suite of programs in combination with the RI[29] technique.

All ground-state and excited-state geometry optimizations were carried out with convergence criteria fixed to 10^{-6} hartree for the energy and <0.001 hartree$\cdot$Å^{-1} for the gradient norm vector. This computational setting[10] provides ground-state geometry parameters in agreement with experimental X-ray values and reasonable results for excited-state PES properties.[30] QTAIM parameters at the density critical point (CP) were computed using the PROAIMV code,[31] while delocalization indexes for closed-shell systems were calculated using the DELIND code.[32] The delocalization index δ(A,B) between the atoms A and B was computed within QTAIM as

$$\delta(\mathrm{A},\mathrm{B}) = -2\sum_{i,j} S_{ij}^{(\mathrm{A})} S_{ij}^{(\mathrm{B})} \tag{1}$$

where the atomic overlap integrals $S_{ij}^{(X)}$ on the ϕ basis set are calculated over the X atomic basis Ω(X) as

$$S_{ij}^{(\mathrm{X})} = \int_{\Omega(\mathrm{X})} \phi_i(\mathbf{r})\phi_j(\mathbf{r})\mathrm{d}\mathbf{r} \tag{2}$$

The δ(A,B) quantity measures the extent of sharing of the electron pairs between two atoms, and it is more formally expressed by the integration of the spinless exchange–correlation pair density $\Gamma_{XC}(\mathbf{r}_1, \mathbf{r}_2)$ over the atomic basins A and B

$$\delta(\mathrm{A},\mathrm{B}) = 2\int_{\Omega(\mathrm{A})}\int_{\Omega(\mathrm{B})} \Gamma_{\mathrm{XC}}(\mathbf{r}_1, \mathbf{r}_2)\mathrm{d}\mathbf{r}_1\mathrm{d}\mathbf{r}_2 \tag{3}$$

where $\Gamma_{XC}(\mathbf{r}_1,\mathbf{r}_2)$ is the difference between the full pair density $\Gamma(\mathbf{r}_1,\mathbf{r}_2)$ and the uncorrelated pair density $\rho(\mathbf{r}_1)\rho(\mathbf{r}_2)$. This parameter has been associated with the c*ovalent* bond order and has been successfully employed for the characterization of chemical bonds in transition-metal carbonyl complexes.[33−35]

3. Results

3.1. Singlet Ground-State Forms. Geometry optimizations were carried out imposing C_s symmetry. Complete active space SCF (CASSCF) single-point energies at the BP86-optimized structure were computed, analyzing the occupation numbers of the active MO in order to evaluate the multireference character

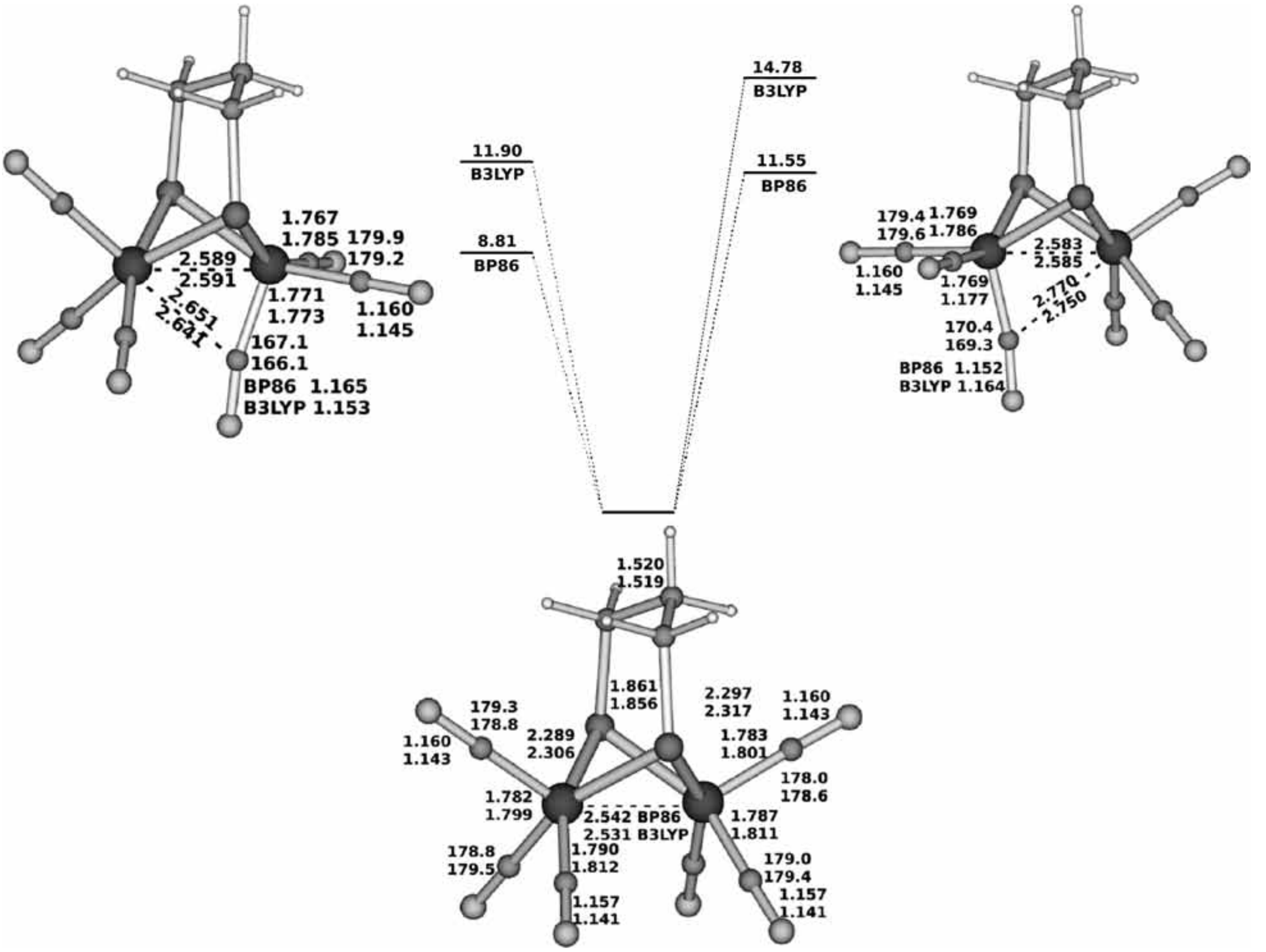

Figure 1. BP86/TZVP and B3LYP/TZVP free-energy diagram and optimized geometry parameters of the $^1\mathbf{a}$ ground-state and $Fe(CO)_3$ rotational transition-state $^1\mathbf{a}_{syn}$ and $^1\mathbf{a}_{anti}$ structures. Free energies are in kcal·mol^{-1}, distances are given in Å, and angles are given in degrees. The experimental geometry parameters are Fe−Fe 2.485 Å (EXAFS), 2.5103 Å (XRD); Fe−S 2.241 Å (EXAFS), 2.2542 and 2.2491 Å (XRD); Fe−C_{eq} 1.786 Å (EXAFS), 1.797 and 1.801 Å (XRD); Fe−C_{ax} 1.802 Å (XRD); C−O_{eq} 1.157 Å (EXAFS), 1.141 and 1.136 Å (XRD); and Fe−C_{ax} 1.130 Å (XRD). Experimental free-energy barriers (ref 41): 10.44 kcal·mol^{-1} for anti and 10.38 kcal·mol^{-1} for syn.

of the wave functions.[36] The computational details and results of these CASSCF calculations are reported as Supporting Information.

The all-terminal CO form ($^1\mathbf{a}$ hereafter) is a low-spin Fe^IFe^I binuclear complex with the $^1A'$ ground-state electronic molecular term. The CO ligands can be classified as trans or cis relative to μ-pdt; each trans or cis CO group can be further classified as anti or syn with respect to the β carbon of the CH_2 group of μ-pdt (see Chart 3).

BP86- and B3LYP-optimized geometry parameters are reported in Figure 1. On average, BP86-optimized geometries are slightly in better agreement with the EXAFS and XRD experimental geometries. BP86 gives C−O distances shorter than B3LYP, while the opposite is true for Fe−C distances. Both DFT functionals overestimate the Fe−Fe distance compared to experimental values (2.485 Å EXAFS, 2.5103 Å XRD), although B3LYP to a lesser extent. Fe−S distances (2.241 Å EXAFS, 2.2542 and 2.2491 Å XRD) are better reproduced by BP86. The frontier molecular orbitals (FMO) and CO stretching frequencies have already been discussed in the previous theoretical literature.[18,37−40] For the sake of completeness, FMO energies and shapes and CO stretching frequencies are reported in the Supporting Information.

The asymmetry imposed by the μ-pdt group implies the existence of two rotated TSs on the **a** PES (see Chart 2). One of the terminal CO ligands that belongs to the rotated $Fe(CO)_3$ group acquires a semibridging character, while the remaining two CO ligands lie roughly on a plane normal to the σ_h plane. The rotational barriers were determined by ^{13}C dynamical NMR experiments by Lyon et al.[41] and by B3LYP computations.[42]

The semibridging character of the CO ligand is stronger in $^1\mathbf{a}_{syn}$ compared to that in $^1\mathbf{a}_{anti}$ according to (i) the shorter distance (Fe−C_μ hereafter) between the carbon atom of the semibridging ligand and the iron atom that belongs to the unrotated $Fe(CO)_3$ group (0.119 and 0.109 Å shorter in $^1\mathbf{a}_{syn}$ compared to that in $^1\mathbf{a}_{anti}$ at the BP86 and B3LYP levels, respectively) and (ii) the lower semibridging CO stretching mode frequency (1954 (syn) and 1960 (anti) cm^{-1} at BP86; 1934 (syn) and 1944 (anti) cm^{-1} at B3LYP). The Fe−Fe distances are similar in the two structures and increase compared to the ground state (syn: +0.047 Å BP86, +0.060 Å B3LYP; anti: +0.041 Å BP86, +0.054 Å B3LYP).

The free-energy rotational barriers are reported in Table 1. The predicted value for the *syn*-$Fe(CO)_3$ rotation is lower than that of the anti rotation, in agreement both with experimental (10.44 kcal·mol^{-1} anti; 10.38 kcal·mol^{-1} syn[41]) and previously computed values (15.39 kcal·mol^{-1} anti; 13.71 kcal·mol^{-1} syn).[42] There is a systematic overestimation of the $\Delta G^\ddagger$(anti) − $\Delta G^\ddagger$(syn) difference (2.74 kcal·mol^{-1} BP86, 2.88 kcal·mol^{-1} B3LYP, 1.68 kcal·mol^{-1} previous B3LYP[42]) compared with the experimental value (0.06 kcal·mol^{-1}). This discrepancy between computed and experimental values might be due to

TABLE 1: Transition-State Energies and Rotational Barriers for Singlet Rotational Transition States

	E_{BP86}[a]	E_{B3LYP}[a]	i_{BP86}	i_{B3LYP}	$\Delta G^{\ddagger}_{\mathrm{BP86}}$[b]	$\Delta G^{\ddagger}_{\mathrm{B3LYP}}$[b]	$\Delta G^{\ddagger}_{\mathrm{B3LYP}}$[c]	$\Delta G^{\ddagger}_{\mathrm{exp}}$[d]
$^{1}\mathbf{a}$	−4122.9559	−4121.5951						
$^{1}\mathbf{a}_{\mathrm{syn}}$	−4122.9436	−4121.5778	50.6i	45.7i	8.81	11.90	13.71	10.38
$^{1}\mathbf{a}_{\mathrm{anti}}$	−4122.9393	−4121.5732	36.1i	60.9i	11.55	14.78	15.39	10.44
$^{1}\mathbf{a}_{\mathrm{CH_2}}$	−4122.9411	−4121.5793	247.0i	259.6i	9.30	9.76		

[a] Energies in hartree. [b] Barriers for a given DFT functional are in kcal·mol^{-1}. [c] See ref 40. [d] See ref 39.

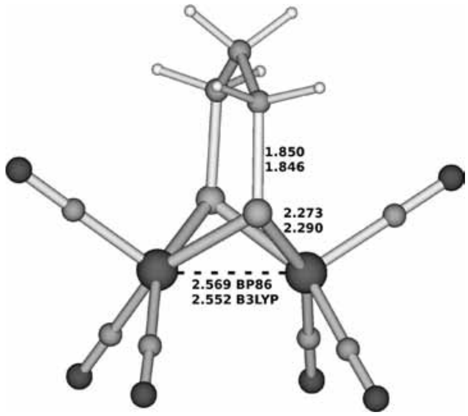

Figure 2. BP86/TZVP- and B3LYP/TZVP-optimized geometry parameters of the $^{1}\mathbf{a}_{\mathrm{CH_2}}$ μ-pdt CH$_2$ flipping C_{2v} TS. The corresponding free-energy barrier and imaginary frequency mode are reported in Table 1.

the fact that the CH$_2$ flipping of the bidentate ligand has a free-energy barrier close to those of the rotations. Figure 2 reports the CH$_2$ flipping TS of C_{2v} symmetry ($^{1}\mathbf{a}_{\mathrm{CH_2}}$). The corresponding barriers are 9.30 and 9.76 kcal·mol^{-1} at the BP86 and B3LYP levels, respectively. We conclude that during dynamical NMR experiments, the CH$_2$ flipping and the Fe(CO)$_3$ rotations take place at similar temperatures, making it difficult to distinguish between the syn and anti rotational processes.

3.2. Structures of $\mathbf{a}^{+}$ and $\mathbf{a}^{-}$ Species.

The $\mathbf{a}^{+}$ (Fe$^{\mathrm{I}}$Fe$^{\mathrm{II}}$) and $\mathbf{a}^{-}$ (Fe$^{\mathrm{I}}$Fe^{0}) PESs were explored using $^{1}\mathbf{a}$ stationary points as starting points for geometry optimizations. In all cases, no symmetry constraints were imposed. Optimized geometry parameters and energy differences between the isomers are reported in Figures 3 and 5.

Roy and co-workers[43] investigated the $\mathbf{a}^{+}$ PES in the frame of the DFT evaluation of the one-electron redox potential for a series of [FeFe] hydrogenase models. These authors observed the stabilization of the syn rotated form by 4 kcal·mol^{-1}. Furthermore, Petro and co-workers,[44] combining photoelectron spectroscopy and DFT computations, estimated the $\mathbf{a}$ reorganization energy[45] to be 12.2 kcal·mol^{-1}.

On the cationic PES, the three stationary points identified (namely, $^{2}\mathbf{a}^{+}$, $^{2}\mathbf{a}_{\mathrm{syn}}^{+}$ and $^{2}\mathbf{a}_{\mathrm{anti}}^{+}$) are all local minima, at variance with the ground-state PES. The $^{2}\mathbf{a}_{\mathrm{syn}}^{+}$ rotated form is the global minimum, which is stabilized by 3.72 (BP86) and 2.61 (B3LYP) kcal·mol^{-1} compared to $^{2}\mathbf{a}^{+}$, in line with previous DFT values[43] and in agreement with the experimental and theoretical findings on other Fe$^{\mathrm{I}}$Fe$^{\mathrm{II}}$ biomimetic complexes.[15,49] Going from Fe$^{\mathrm{I}}$Fe$^{\mathrm{I}}$ to Fe$^{\mathrm{I}}$Fe$^{\mathrm{II}}$, (i) the Fe−Fe distances increase by 0.132 Å for the all-terminal form and only by 0.025 and 0.032 Å for syn and anti forms, respectively, and (ii) Fe−C$_{\mu}$ distances decrease on average by 0.135 Å, indicating the stronger bridging character of the semibridged CO ligand in the rotated cationic species. Going from the rotated to all-terminal form, the Fe−Fe bond distance is shortened (−0.06 Å syn and −0.054 Å anti BP86; −0.044 Å syn and −0.034 Å anti B3LYP).

The $^{2}\mathbf{a}^{+}$ is a local minimum, and therefore, it should have at least one TS that connects each rotated form with $^{2}\mathbf{a}^{+}$. We performed the TS search only at the BP86 level for the $^{2}\mathbf{a}^{+} \rightarrow {}^{2}\mathbf{a}_{\mathrm{syn}}^{+}$ isomerization. The optimized TS structure ($^{2}\mathbf{a}_{\mathrm{TS,syn}}^{+}$ hereafter; imaginary mode frequency: i49.4 cm^{-1}) is reported in Figure 4. This TS can be described as a partially rotated form close to $^{2}\mathbf{a}^{+}$. The *syn*-Fe(CO)$_3$ group is rotated around the Fe−Fe axis and one *trans*-CO ligand acquires a slight bridging character (Fe−C$_{\mu}$ distance 3.049 Å). The three CO ligands do not rotate in the same way, as shown by the values of the C−Fe−Fe−C dihedral angles reported in Figure 4. The predicted free-energy barriers are 4.89 kcal·mol^{-1} for $^{2}\mathbf{a}_{\mathrm{syn}}^{+} \rightarrow {}^{2}\mathbf{a}^{+}$ isomerization and 1.54 kcal·mol^{-1} for $^{2}\mathbf{a}^{+} \rightarrow {}^{2}\mathbf{a}_{\mathrm{syn}}^{+}$.

The radical anionic $\mathbf{a}^{-}$ species can be obtained by reduction of $\mathbf{a}$ and has been characterized by spectrochemical investigation.[9,50] The $\mathbf{a}^{-}$ and $\mathbf{a}$ PESs (see Figure 5) are similar. The all-terminal CO structure ($^{2}\mathbf{a}^{-}$) is found to be the global minimum, while the rotated forms ($^{2}\mathbf{a}_{\mathrm{syn}}^{-}$ or $^{2}\mathbf{a}_{\mathrm{anti}}^{-}$) have C_s symmetry and are first-order saddle points that are higher in energy (imaginary mode frequencies: i39.5 (BP86) and i44.9 (B3LYP) cm^{-1} for $^{2}\mathbf{a}_{\mathrm{anti}}^{-}$; i31.0 (BP86) and i36.3 (B3LYP) cm^{-1} for $^{2}\mathbf{a}_{\mathrm{syn}}^{-}$).

3.3. Fe−Fe, Fe−C$_{\mu}$, and Fe−O$_{\mu}$ Interaction Properties.

The characterization of the metal−metal bond in transition-metal complexes is a long-standing problem, which has been addressed using different approaches. In the present paper, we employed the analysis of the theoretical electron density within the Quantum Theory of Atom in Molecules (QTAIM).[52,53] Besides the QTAIM topological indexes usually employed for the characterization of the chemical bonds (electron density ρ_{bcp}, its laplacian $\nabla^2\rho_{\mathrm{bcp}}$, and the energy density H_{bcp} at the bond critical point (BCP)[51]), we computed the delocalization index δ(A,B), which is often more effective in the description of metal−metal bonds in transition-metal complexes.[33] This analysis was employed on the BP86 electron density. For $^{1}\mathbf{a}$, $^{1}\mathbf{a}_{\mathrm{syn}}$, and $^{1}\mathbf{a}_{\mathrm{anti}}$ BP86 structures (see Table 2), the Fe−Fe bond critical point (BCP) was always found closer to Fe$_1$ (Fe$_1$-BCP, 1.155 Å; BCP-Fe$_2$, 1.409 Å, for $^{1}\mathbf{a}$ and similarly for $^{1}\mathbf{a}_{\mathrm{syn}}$ and $^{1}\mathbf{a}_{\mathrm{anti}}$) and placed slightly above the Fe−Fe internuclear axis toward the μ-pdt bridge. The higher Fe−Fe ρ_{bcp} value for the all-terminal form compared to those of the rotated forms indicates the weakening of the Fe−Fe bond for the latter. The difference between *syn*- and *anti*-Fe−Fe ρ_{bcp} values (0.04) is too small to comment.

The positive but small values of $\nabla^2\rho_{\mathrm{bcp}}$ (indicating closed-shell bond interaction) and, at the same time, the negative but small values of H_{bcp} (indicating shared-shell bond interaction) highlight the difficulties in the characterization of the nature of this Fe−Fe bond (see Table 2). However, the delocalization index δ(Fe,Fe) better evidences the nature of this bond (see Figure 6). The delocalization between the two iron atoms is partial and decreases in the TS structures, likely due to formation of a weak interaction between the unrotated Fe atom and the C$_{\mu}$ atom. All δ(Fe,Fe) values obtained are lower than 0.5 (where a value of 1 as in H$_2$ or 1.03 for the C−C bond in ethane indicates a formal single covalent bond) and close to that of Fe$_2$(CO)$_9$ (δ(Fe,Fe) = 0.335,[33] 0.4,[35] and 0.456 BP86/TZVP).

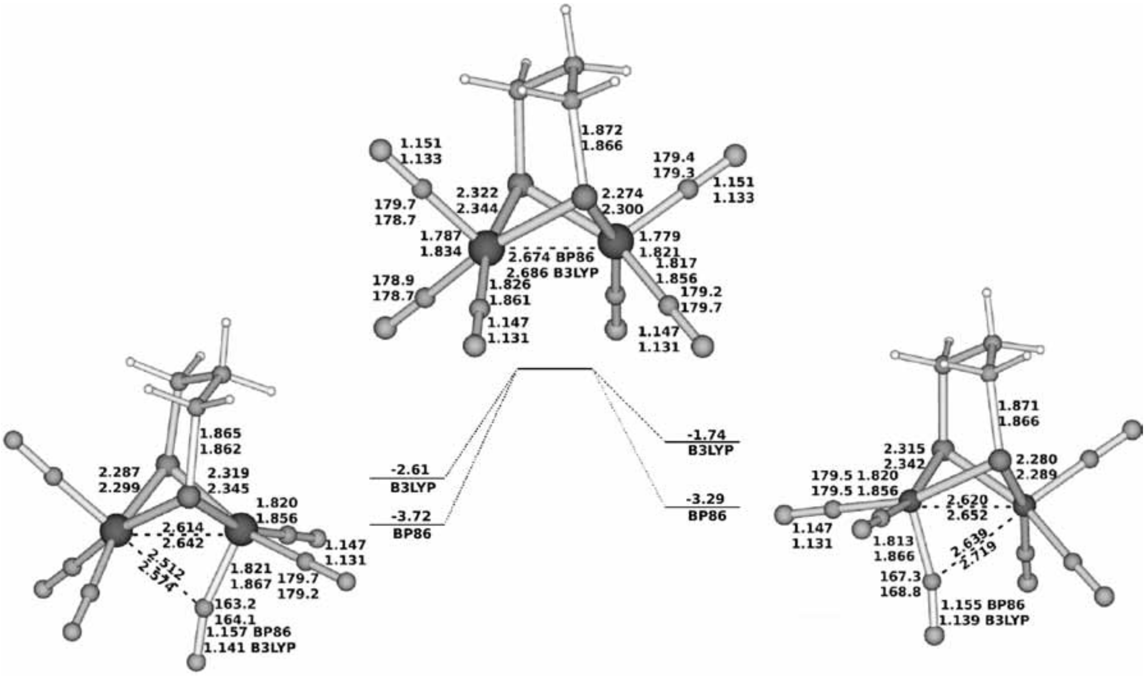

Figure 3. BP86/TZVP and B3LYP/TZVP energy diagrams and optimized geometry parameters of the cationic $^2\mathbf{a}_{syn}{}^+$ global minimum and the two local minima $^2\mathbf{a}^+$ and $^2\mathbf{a}_{anti}{}^+$. Energies are in kcal·mol^{-1}, distances are given in Å, and angles are given in degrees.

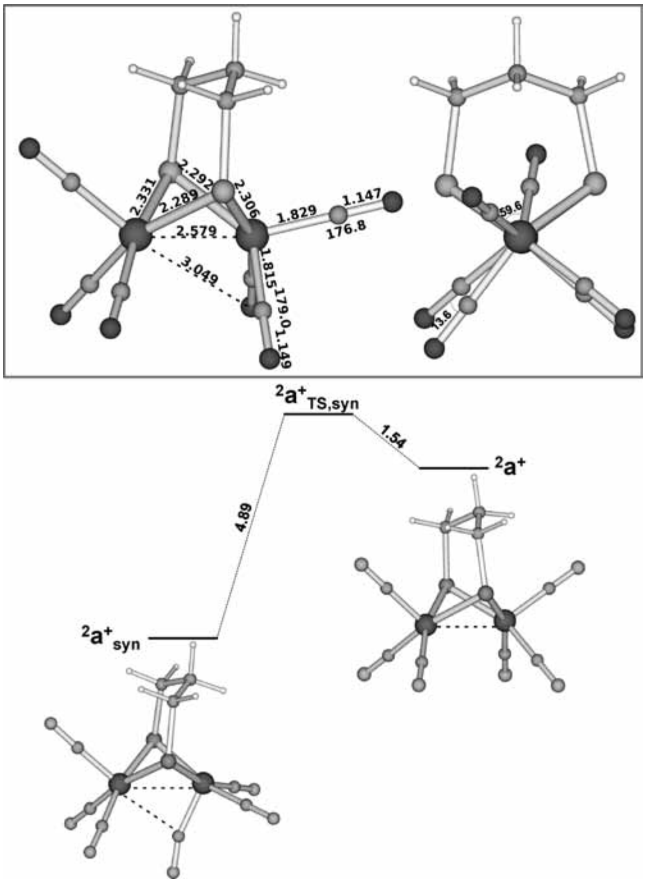

Figure 4. Optimized geometry parameters of the $^2\mathbf{a}_{syn}{}^+ \rightarrow {}^2\mathbf{a}^+$ TS ($^2\mathbf{a}_{TS,syn}{}^+$) at the BP86/TZVP level. Distances are given in Å, and angles are given in degrees. Free-energy barriers are given in kcal·mol^{-1}.

As suggested by Gatti et al.,[33] a similar bond situation can be pictured as "a non localized M−M interaction, with features very different from those of a typical single covalent bond". Concerning the rotated forms, although no Fe−C$_\mu$ BCP was found, the values of the δ(Fe,C$_\mu$) index indicate a weak but significant interaction if compared with the value computed for the fully bridged CO group (0.629) in $Fe_2(CO)_9$ and the almost terminal CO in D_{3d} $Co_2(CO)_8$(0.07).[34]

In general, the π-back-donation between transition-metal atoms and the CO includes a significant metal−oxygen interaction that can be detected by computing the delocalization indexes δ(Fe,O).[34] In order to better understand this analysis, we first consider D_{3h} tribridged $Fe_2(CO)_9$ to understand the δ(Fe,O) behavior as a function of the CO bonding mode. The fully bridged CO ligand is characterized as having the two δ(Fe,O)'s equal to each other ($\delta(Fe,O_\mu) = 0.130$ BP86/TZVP each), suggesting an equal π-back-donation from each metal atom. When a terminal CO is considered, only the Fe atom to which the ligand is bound back-donates, with $\delta(Fe,O) = 0.180$. If we consider the sum of the δ(Fe,O) as a measure of the metal atom back-donation capacity, this increases going from the terminal (0.180) to bridged CO ligand (0.260). For the two rotated forms (see Figure 7), the π-back-donation is mainly due to the iron atom that belongs to the rotated $Fe(CO)_3$, as suggest by the very low value of the $\delta(Fe,O_\mu)$ computed for the iron atom that belongs to the unrotated $Fe(CO)_3$. This trend is similar to that found for the terminal CO in $^1\mathbf{a}$, in which the back-donation from the Fe atom not bound to the CO ligand is almost negligible. Finally, the sum of the δ(Fe,O) values going from the terminal to semibridged CO ligand (all-terminal 0.215, syn 0.265, anti 0.262) increases to a lesser extent with respect to $Fe_2(CO)_9$.

We now consider the cationic and anionic forms. The Fe−Fe bonding interaction for the all-terminal form ($^2\mathbf{a}^+$) is the weakest among those of the cationic forms (see Figure 8). This observation is corroborated by the fact that upon oxidation, the Fe−Fe $^1\mathbf{a}$ BCP becomes a (3,+1) ring critical point in $^2\mathbf{a}^+$. On the contrary, the Fe−Fe BCP is found either in $^2\mathbf{a}_{syn}{}^+$ or $^2\mathbf{a}_{anti}{}^+$, although with lower ρ_{bcp} values with respect to $^1\mathbf{a}_{syn}$ and $^1\mathbf{a}_{anti}$. Fe−Fe bond interactions are further weakened in the anionic structures compared to those of the corresponding cationic forms. Fe−Fe distances increase in the rotated structures

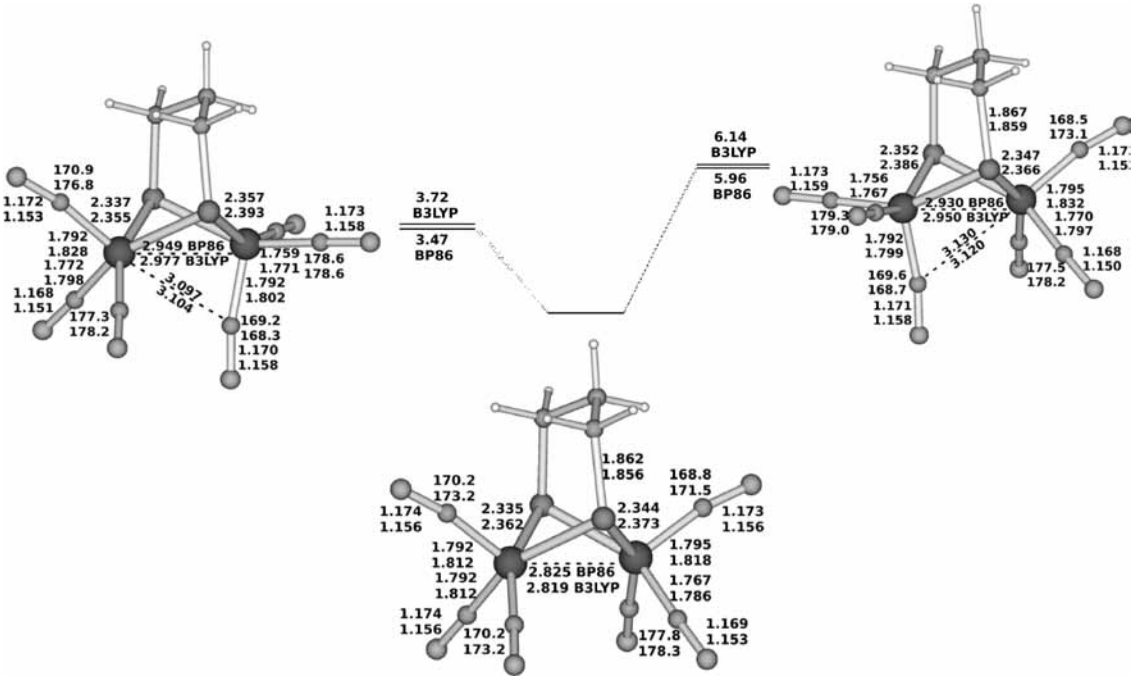

Figure 5. BP86/TZVP and B3LYP/TZVP energy diagrams and optimized geometry parameters of the anionic $^2\mathbf{a}^-$ global minima and the two $Fe(CO)_3$ rotational TSs ($^2\mathbf{a}_{syn}^-$ and $^2\mathbf{a}_{anti}^-$). Energies are in kcal·mol^{-1}, distances are given in Å, and angles are given in degrees.

TABLE 2: Topological Fe−Fe Bond Properties at the Fe−Fe Bond Critical Point, Fe Atomic Net Charges, and Fe−Fe and Fe−C$_\mu$ Delocalization Indexes for the Neutral, Cationic, and Anionic a PES Stationery Points Computed from the BP86 Wave Funtion

	R(Fe−Fe)^a	q(Fe$_1$)^b	q(Fe$_2$)^b	$\rho_{bcp} \times 10^{2c}$	$\nabla^2\rho_{bcp} \times 10^{2c}$	$H_{bcp} \times 10^{2c}$	δ(Fe−Fe)^d	δ(Fe−C$_\mu$)^d
$^1\mathbf{a}$	2.542	0.686	0.694	4.73^e	6.48	−1.10	0.471	
$^1\mathbf{a}_{syn}$	2.589	0.737	0.698	4.34^e	6.50	−0.94	0.384	0.202
$^1\mathbf{a}_{anti}$	2.583	0.689	0.733	4.38^e	6.29	−0.96	0.411	0.162
$^2\mathbf{a}^+$	2.674	0.757	0.751	3.81^f				
$^2\mathbf{a}_{syn}^+$	2.620	0.784	0.776	4.15^e	7.31	−0.84		
$^2\mathbf{a}_{anti}^+$	2.614	0.760	0.789	4.12^e	7.23	−0.82		
$^2\mathbf{a}^-$	2.825	0.722	0.720	3.18^f				
$^2\mathbf{a}_{syn}^-$	2.949	0.758	0.719	2.98^f				
$^2\mathbf{a}_{anti}^-$	2.930	0.713	0.759	2.98^f				

[a] Distance in Å. [b] The 1 and 2 subscripts indicate the iron atom that belongs to the *anti*- or *syn*-$Fe(CO)_3$ group, respectively. [c] All topological parameters in atomic units. [d] Fe−Fe and Fe−C$_\mu$ delocalization indexes (see text for details). [e] The (3,−1) bond critical point (BCP). [f] The (3,+1) ring critical point (RCP).

compared to those of $^2\mathbf{a}^-$ (at the BP86 level, 0.124 Å syn and 0.105 Å anti; at the B3LYP level, 0.158 Å anti and 0.131 Å anti). All Fe−Fe BCPs become RCPs with the ρ_{cp} values roughly decreased by 30% compared with the corresponding values for the neutral species.

QTAIM atomic net charges are collected in Figure 9. Some general trends are observed in the iron charge values in going from the syn to the anti form, no matter which is the total charge of the system considered. The charge of the iron atom that belongs to unrotated $Fe(CO)_3$ group is always slightly more positive that that of the iron atom that belongs to the rotated $Fe(CO)_3$ group, at variance with Mulliken charges.[42] The positive charge of the carbon atom of the semibridged CO ligand (C$_\mu$) is always lower than that of the terminal CO ligand. These results testify to the shift of the electron density from the unrotated Fe to the C$_\mu$ atom to form a weak Fe−C$_\mu$ interaction. Going from the cationic to the anionic PES, the variations of the charges are delocalized on the whole molecules. In particular the positive Fe charge decreases on average by 0.055, while the two sulfur atoms increase their negative charge (−0.05 on average).

3.4. Excited States. In this section, we report the results of the explorations of the first four singlet excited-state and of two high-lying excited-state PESs carried out using the TDDFT and BP86 functional. Five excited states above the one under investigation were also included in the TDDFT energy computations in order to ensure a better convergence of the geometry optimization. For lowest triplet state PES exploration, geometry optimizations were performed using DFT without any symmetry constraints.

3.4.1. Singlet Excited States. The UV−vis electronic spectra of $^1\mathbf{a}$ have been previously published by Lyon et al.[41] and Fiedler et al.[18] The spectrum exhibits a weak intensity shoulder at ∼461 nm and an intense band at 327−329 nm. According to the TDDFT/B3LYP-computed spectra,[18] the absorptions below ∼312 nm mainly involve Fe−Fe 3d orbitals. In particular, (i) the weak band at ∼461 nm is assigned to the HOMO-2 → LUMO excitation, and (ii) the intense band is assigned to the HOMO → LUMO excitation. Finally, the absorptions above ∼312 nm are Fe → CO metal-to-ligand charge-transfer excitations.

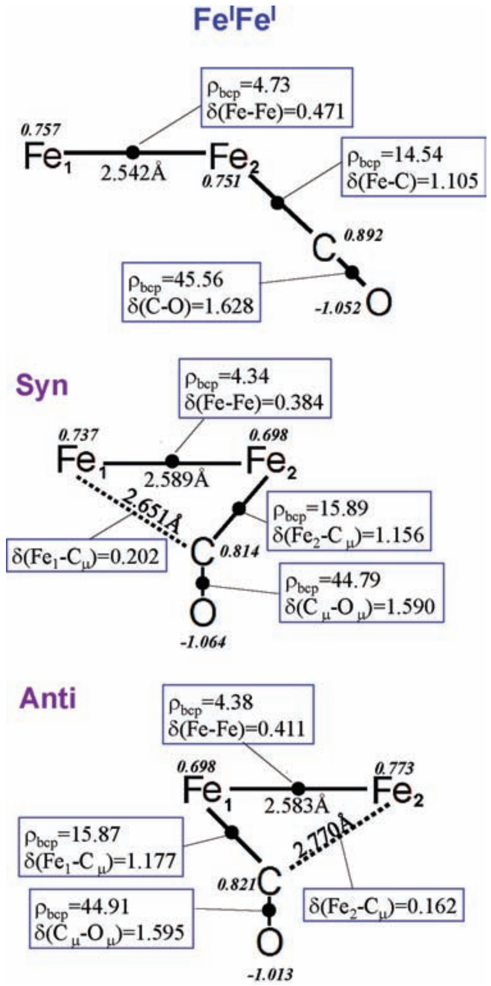

Figure 6. QTAIM parameter for $Fe_2(S_2C_3H_6)(CO)_6$ all-terminal CO and the $Fe(CO)_3$ rotated structures. Close circles indicate the (3,−1) bond critical point. Electron densities at the critical point in atomic units are $\times 10^2$; atomic net charges are reported in italic; distances are in Å.

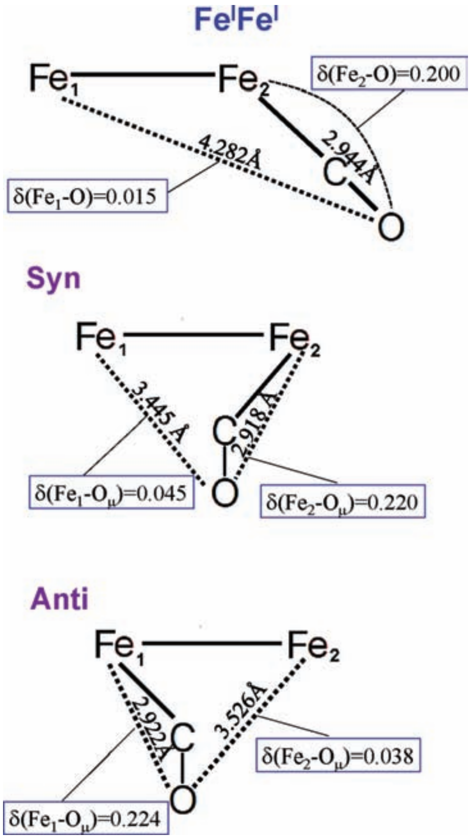

Figure 7. The δ(Fe−O) delocalization parameters for $Fe_2(S_2C_3H_6)(CO)_6$ all-terminal CO and the $Fe(CO)_3$ rotated structures. Distances are in Å. For sake of comparison, for tribridged D_{3h} $Fe_2(CO)_9$ (BP86/TZVP), both $\delta(Fe-O_\mu)$ values are equal to 0.130 for the fully bridged CO, while δ(Fe−O) = 0.180 for the terminal CO.

In Table 3, are reported the BP86 vertical excitation energies in the range between 440 and 300 nm, together with the corresponding oscillation strenghts and one-electron excitation major percentage contributions. The first four excited states are characterized by the HOMO-*n* → LUMO (62a′) leading one-electron excitation, and according to the FMO orbital compositions (see Supporting Information), they show a small CT character. These excitations can be assigned to the weak intensity shoulder of the spectrum centered around the most intense band ($2^1A'$, 408.7 nm). Higher-energy excited states are mainly characterized by the HOMO-*n* → LUMO+1 (36a″) and HOMO-*n* → LUMO+2 (37a″) one-electron excitations. Since these two virtual MOs (see Supporting Information) are basically ligand based, these transitions show a larger CT character (mainly of Fe → S and Fe−CO type). Among these transitions, the most intense are the $3^1A'$ and the $4^1A'$ (382.3 and 369.9 nm, respectively). This assignment is in agreement with that proposed by Fiedler et al.[18] on the basis of TDDFT/B3LYP computations. In order to asses the reliability of the BP86 results obtained, the excitation energies and state compositions were computed also using B3LYP and PBE0[46] hybrid functionals because of their better performance (in particular, PBE0[47]) in evaluating charge-transfer state energies[48] (see the Supporting Information for the computational details and tables). The comparison between the computed and experimental excitation energies gave evidence that the weak intensity shoulder is better reproduce by BP86, while the transitions that correspond to the intense band are better reproduce by hybrid functionals (in particular by PBE0) because of their larger CT character. Finally, all functionals considered computed the HOMO → LUMO transition to be higher in energy with respect to the HOMO-*n* → LUMO transitions. As previously commented,[18] this can be attributed to the lack of orbital relaxation in TDDFT.

Low-lying and high-lying excited-state optimized structures are reported in Figures 12 and 13, respectively.

$1^1A''$. This is the lowest-energy singlet excited state, according to the computed BP86 vertical excitation energy (see Table 3). The leading one-electron excitation is HOMO-2 (35a″) → LUMO (62a′), where the HOMO-2 has Fe−S bonding character. Starting from the ^{1}**a** structure, a stationary point was found with a particular *anti*-$Fe(CO)_3$ semirotated ligand arrangement similar to that found for $^2\mathbf{a}_{TS,syn}{}^+$. The C−Fe−Fe−C dihedral formed by the Fe−C bonds of the two axial CO ligands is 43.1° (instead of 0 in ^{1}**a** and 93° in $^1\mathbf{a}_{anti}$), while the Fe−Fe bond distance is longer by 0.363 Å then that in ^{1}**a**. Also, Fe−S distances are elongated, but to a lesser extent (on average only 0.018 Å). Starting from $^1\mathbf{a}_{syn}$ and $^1\mathbf{a}_{anti}$, after a few tens of cycles, the geometry started fluctuating without further evolution, and no stationary points were found. We further explored this PES by imposing C_s symmetry at the TDDFT level, finding two stationary points (geometry not reported) higher in energy compared to the semirotated structure described above. Finally, we imposed C_s symmetry and the proper MO occupancy in order to constrain the wave function to the $^1A''$ electronic term, allowing us to use DFT instead of TDDFT to compute normal-

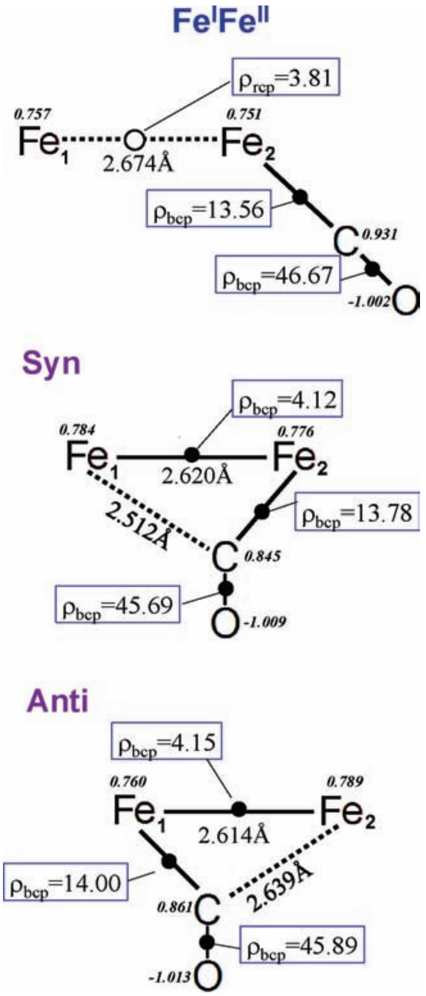

Figure 8. QTAIM parameter for $Fe_2(S_2C_3H_6)(CO)_6^+$ all-terminal CO and the $Fe(CO)_3$ rotated structures. Open and close circles indicate the (3,+1) ring critical point and the (3,−1) bond critical point. The electron density at the critical point is atomic units × 10^2; atomic net charges are reported in italic; distances are in Å.

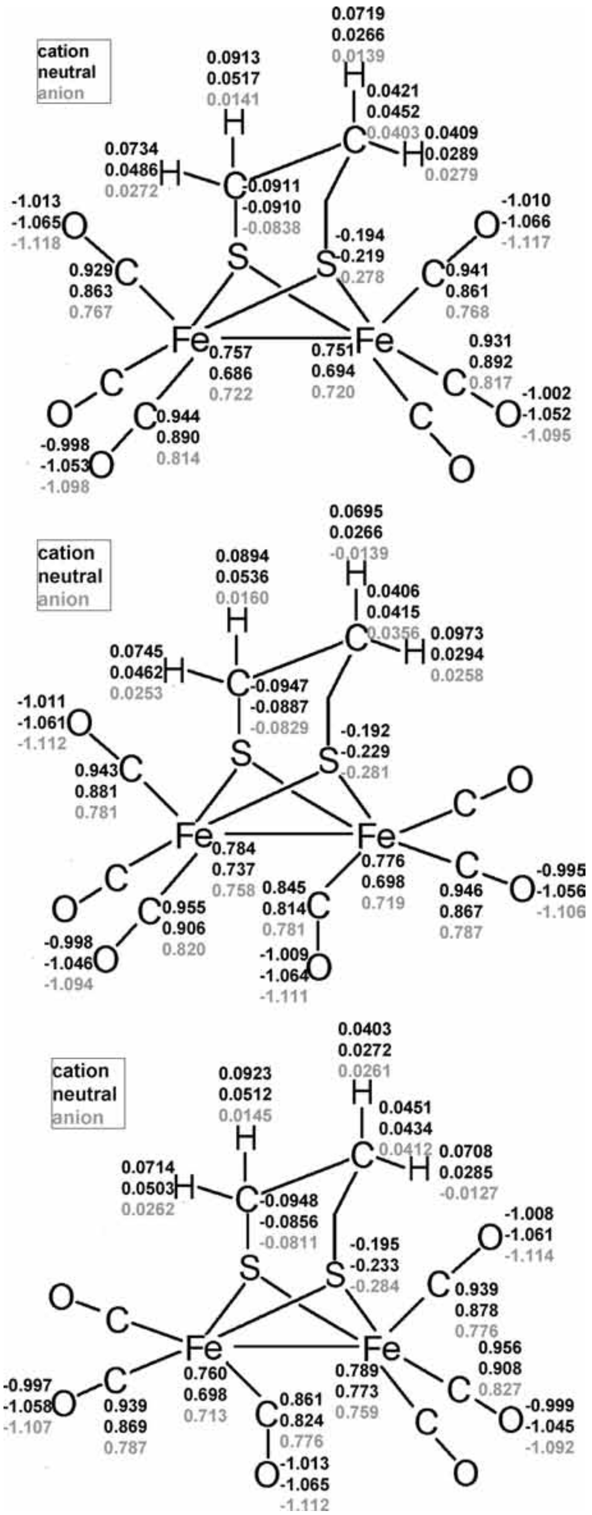

Figure 9. The **a**, **a**$^+$, and **a**$^-$ PES stationary point QTAIM atomic net charges computed using the BP86/TZVP electron density.

mode frequencies. We found that either the rotated structures or the all-terminal structure are transition states.[54] These observations allow us to claim with more confidence that the structure proposed in Figure 12 is a genuine minimum of the $1^1A''$ PES and likely the global minimum or a structure very close to it.

$1^1A'$. When the all-terminal CO structure is considered, the leading one-electron excitation is the HOMO-1 (60a″) → LUMO (62a′) (% contribution equal to 72.8), where HOMO-1 has a stronger Fe−S bonding character than HOMO-2. The contribution of the HOMO (61a″) → LUMO (62a′) excitation is smaller (21.7%) but increases to 100 (anti) and 88.5% (syn) when rotated structures are considered. This fact is mainly due to the decreasing of the HOMO/LUMO gap in $^1\mathbf{a}_{syn}$ and $^1\mathbf{a}_{anti}$ compared with that of $^1\mathbf{a}$. Geometry optimization carried out without symmetry constraints failed to meet convergence criteria due to oscillation behavior. When the C_s symmetry was imposed, three stationary points were found. The anti rotated structure is the lowest energy form, and the all-terminal CO structure lies 3.9 kcal·mol^{-1} higher in energy. The Fe−Fe distances increase compared with those of the corresponding ground-state forms (+0.254 Å for all-terminal CO structure, +0.289 Å for the anti rotated structure, and +0.254 Å for the syn rotated structure). For the all-terminal structure, the *anti*-Fe−S distance is elongated by 0.094 Å, and both Fe−C−O angles for *cis*-CO ligands are bent 15.6 (anti) and 7.4° (syn) out of linearity, and the corresponding Fe−C distances are increased (+0.067 Å anti; +0.013 Å syn). A similar situation is also found for the rotated structures, although to a lesser extent. These results are easily explained considering that the LUMO has antibonding character with respect to both Fe−Fe and Fe−C_{cis} bonds.

$2^1A'$. The leading one-electron excitation is HOMO-4 (59a′) → LUMO (62a′), where HOMO-4 has strong contributions from the sulfur orbitals, with a Fe−S bonding character. No geometry optimizations performed either with or without symmetry

TABLE 3: Computed Excited-State Energies, State Composition, and Oscillation Strength for a

	E_{vertical}[a]	nm[b]	f[c]	1e[d]	E_1[e]	grad_1[f]	E_{anti}[e]	$\mathrm{grad}_{\mathrm{anti}}$[f]	E_{syn}[e]	$\mathrm{grad}_{\mathrm{syn}}$[f]
$^1A'$	−4122.9559									
$1^1A''$	−4122.8510	434.1	2×10^{-5}	$35a'' \rightarrow 62a'$	−4122.8912	0.0003				
$1^1A'$	−4122.8501	430.5	4×10^{-3}	72.8 $60a' \rightarrow 62a'$ 21.7 $61a' \rightarrow 62a'$	−4122.8705	0.0005	−4122.8767	0.0005	−4122.8734	0.0003
$2^1A'$	−4122.8445	408.7	7×10^{-3}	54.9 $59a' \rightarrow 62a'$ 23.4 $61a' \rightarrow 62a'$ 13.4 $60a' \rightarrow 62a'$			−4122.8696	0.0005		
$2^1A''$	−4122.8442	407.8	5×10^{-4}	82.5 $35a'' \rightarrow 62a'$ 14.9 $61a' \rightarrow 36a''$	−4122.8550	0.0005	−4122.8610	0.0004	−4122.8604	0.0005
$3^1A''$		400.0	2×10^{-4}	80.4 $61a' \rightarrow 36a''$ 13.2 $34a'' \rightarrow 62a'$						
$4^1A''$		386.8	8×10^{-4}	$61a' \rightarrow 37a''$						
$3^1A'$		382.3	0.01	31.2 $59a' \rightarrow 62a'$ 21.7 $35a'' \rightarrow 36a''$ 13.2 $61a' \rightarrow 62a'$ 11.4 $35a'' \rightarrow 37a''$						
$4^1A'$		369.9	0.01	63.5 $58a' \rightarrow 62a'$ 16.2 $57a' \rightarrow 62a'$						
$5^1A''$		369.4	1×10^{-3}	87.8 $60a' \rightarrow 36a''$ 7.1 $60a' \rightarrow 37a''$						
$5^1A'$		365.3	4×10^{-4}	65.1 $57a' \rightarrow 62a'$ 21.7 $58a' \rightarrow 62a'$						
$6^1A''$		363.1	1×10^{-3}	87.9 $60a' \rightarrow 37a''$ 7.1 $60a' \rightarrow 36a''$						
$6^1A'$	−4122.8276	355.0	7×10^{-3}	37.0 $35a'' \rightarrow 37a''$ 36.4 $35a'' \rightarrow 36a''$	−4122.8373	0.0002				
$7^1A''$		354.2	1×10^{-3}	$59a' \rightarrow 36a''$						
$7^1A'$		346.7	2×10^{-3}	81.0 $34a'' \rightarrow 36a''$ 11.2 $35a'' \rightarrow 36a''$						
$8^1A''$		346.1	1×10^{-3}	$59a' \rightarrow 37a''$						
$8^1A'$		338.1	1×10^{-3}	82.1 $34a'' \rightarrow 37a''$ 9.8 $35a'' \rightarrow 37a''$						
$9^1A''$		335.7	1×10^{-4}	$58a' \rightarrow 36a''$						
$10^1A''$		328.4	1×10^{-4}	54.6 $33a'' \rightarrow 62a'$ 25.4 $58a' \rightarrow 37a''$ 13.9 $57a' \rightarrow 36a''$						
$9^1A'$	−4122.8167	327.2	0.121	24.0 $35a'' \rightarrow 37a''$ 19.6 $61a' \rightarrow 62a'$ 12.1 $35a'' \rightarrow 36a''$ 8.4 $61a' \rightarrow 64a'$	−4122.8224	0.0009				
$11^1A''$		325.8	3×10^{-3}	63.2 $57a' \rightarrow 37a''$ 19.8 $33a'' \rightarrow 62a'$ 14.6 $58a' \rightarrow 37a''$						
$12^1A''$		317.7	$3 \cdot 10^{-3}$	73.5 $57a' \rightarrow 36a''$ 12.3 $33a'' \rightarrow 62a'$						
$13^1A''$		315.1	4×10^{-3}	51.1 $58a' \rightarrow 37a''$ 29.4 $57a' \rightarrow 37a''$ 10.9 $33a'' \rightarrow 62a'$						
$10^1A'$		314.8	6×10^{-3}	87.7 $61a' \rightarrow 63a'$						

[a] E_{vertical} is the vertical energy in hartree. [b] The nm is the excitation energy in nm. [c] The f is the oscillation strength. [d] The leading one-electron excitation refers to the single-excitation contribution a → i. [e] E_1, E_{anti}, and E_{syn} are the energies (in hartrees) of the geometry-optimized excited state structures for the all-terminal, anti, and syn isomers, respectively. [f] Gradient norm vector in hartree Å^{-1}.

constraints converged to a stationary point,[63] except for the C_s anti rotated structure, with an Fe−Fe distance of 2.652 Å, while the *anti*-Fe−S distance equal to 2.399 Å is the longest among all of the structures considered in this paper. Also the *syn−cis*-Fe−C distance is strongly elongated (+0.087 Å compared to that of ^{1}**a**).

$2^1A''$. For all of the isomers considered (all-terminal or rotated), HOMO-2 ($35a''$) → LUMO ($62a'$) (82.5% all-terminal; 60.0% *a*nti and syn) is the leading one-electron excitation. The geometry optimizations were carried out imposing C_s symmetry, except for the syn structures. The syn stationary point is the lowest in energy, although the anti form is only 0.4 kcal·mol^{-1} higher in energy. The all-terminal CO form lies 3.7 kcal·mol^{-1} higher in energy with respect to the syn form. The structures identified are not significantly dissimilar from those previously identified on the $1^1A'$ PES, except for the Fe−Fe distances, which were shorter.

High-Lying Excited States: $6^1A'$ and $9^1A'$. We considered two singlet transitions ($6^1A'$, 355 nm; $9^1A'$, 327 nm), which are likely involved in the CO photolysis experiments.[19,20] The leading one-electron excitations of these states are mainly of HOMO-*n* → LUMO+1/+2 type. Either for the all-terminal or the rotated forms, these MOs are characterized by *trans*-Fe−C antibonding orbital combinations. TDDFT geometry optimizations converge to a stationary point only for the all-terminal forms, which are reported in Figure 12. During the geometry optimization of the rotated forms, the excited-state energies were found always higher than those obtained for the all-terminal form, suggesting a stabilization of the latter, at variance with the cases of the low-lying excited-state PES illustrated above. However, upon analyzing optimization runs of the rotated forms, we found that syn forms are lower in energy (+4.8 ($6^1A'$) and +2.7 kcal·mol^{-1} ($9^1A'$) compared with the all-terminal forms), with significant *anti*−*trans*-Fe−C elongations (+0.051 Å, $6^1A'$; +0.055 Å $9^1A'$).

3.4.2. Lowest Triplet State. The lowest triplet state ($^3A'$ electronic terms) and $\mathbf{a}^+$ are similar (see Figure 10). The all-terminal ($^3\mathbf{a}$) and the anti and syn rotated forms ($^3\mathbf{a}_{\mathrm{anti}}$ and $^3\mathbf{a}_{\mathrm{syn}}$) represent minimum conformations, the latter being the global minimum-energy structure. We have computed the adiabatic energy difference between singlet and triplet states as

$$\Delta E_{\mathrm{triplet-singlet}} = E_{\mathrm{triplet}}(\mathbf{R}_{\mathrm{eq}}^{\mathrm{triplet}}) - E_{\mathrm{singlet}}(\mathbf{R}_{\mathrm{eq}}^{\mathrm{singlet}}) \qquad (4)$$

where the vector $\mathbf{R}_{\mathrm{eq}}$ collects the minimum geometry parameters. As already pointed out,[55] B3LYP stabilizes the singlet low-spin state to a lesser extent compared with BP86; the adiabatic energy differences between the singlet and triplet are 31.9 and 16.5 kcal·mol^{-1} at BP86 and B3LYP, respectively. The adiabatic energy differences for the two rotated forms strongly depend on the DFT functional (syn: 21.59 kcal·mol^{-1} BP86, 2.95 kcal·mol^{-1} B3LYP; anti: 19.08 kcal·mol^{-1} BP86, 1.07

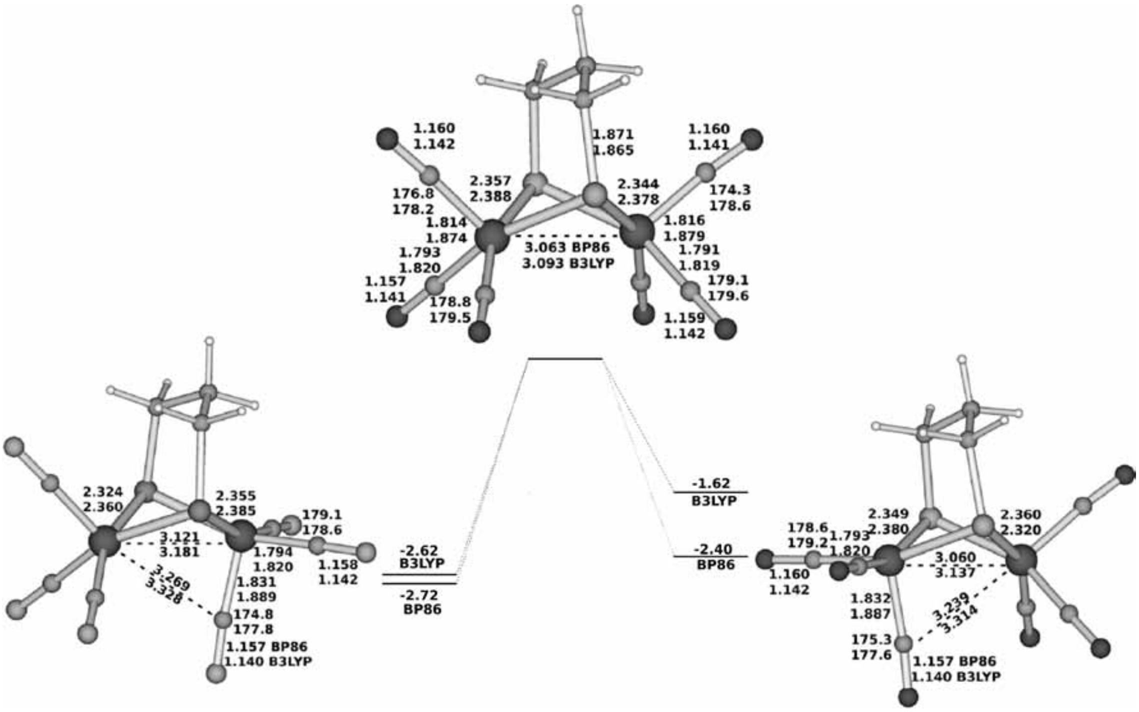

Figure 10. BP86/TZVP and B3LYP/TZVP energy diagram and optimized geometry parameters of $^3\mathbf{a}$ ground-state and Fe(CO)$_3$ rotational $^3\mathbf{a}_{\mathrm{syn}}$ and $^3\mathbf{a}_{\mathrm{anti}}$ structures. Energies are in kcal·mol^{-1}, distances are given in Å, and angles are given in degrees.

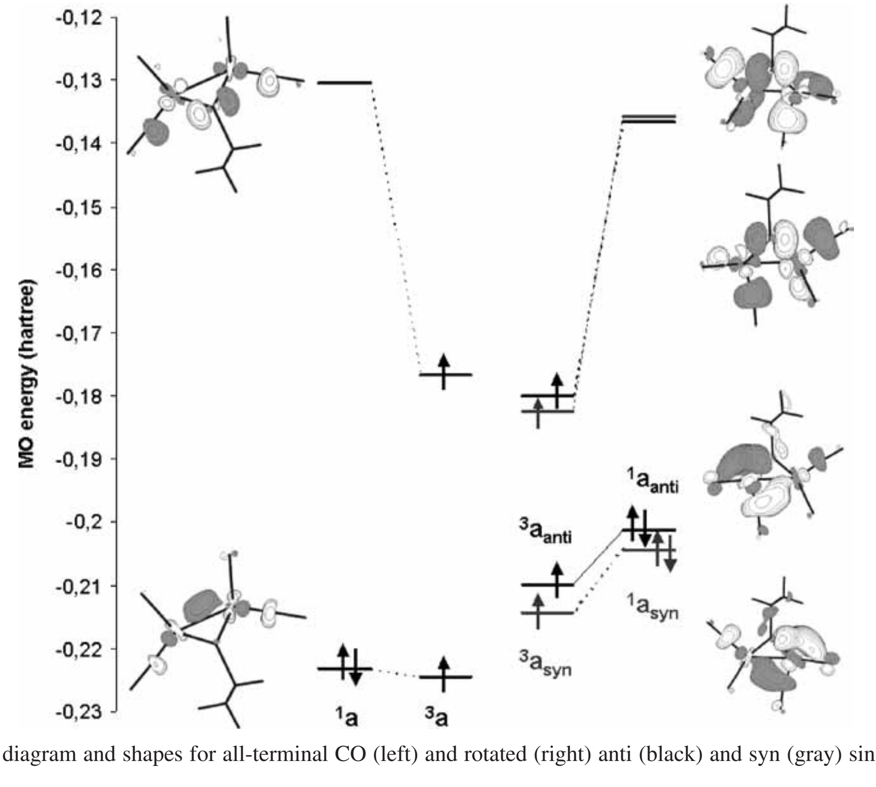

Figure 11. FMO energy diagram and shapes for all-terminal CO (left) and rotated (right) anti (black) and syn (gray) singlet and triplet structures. Energies are in hartree.

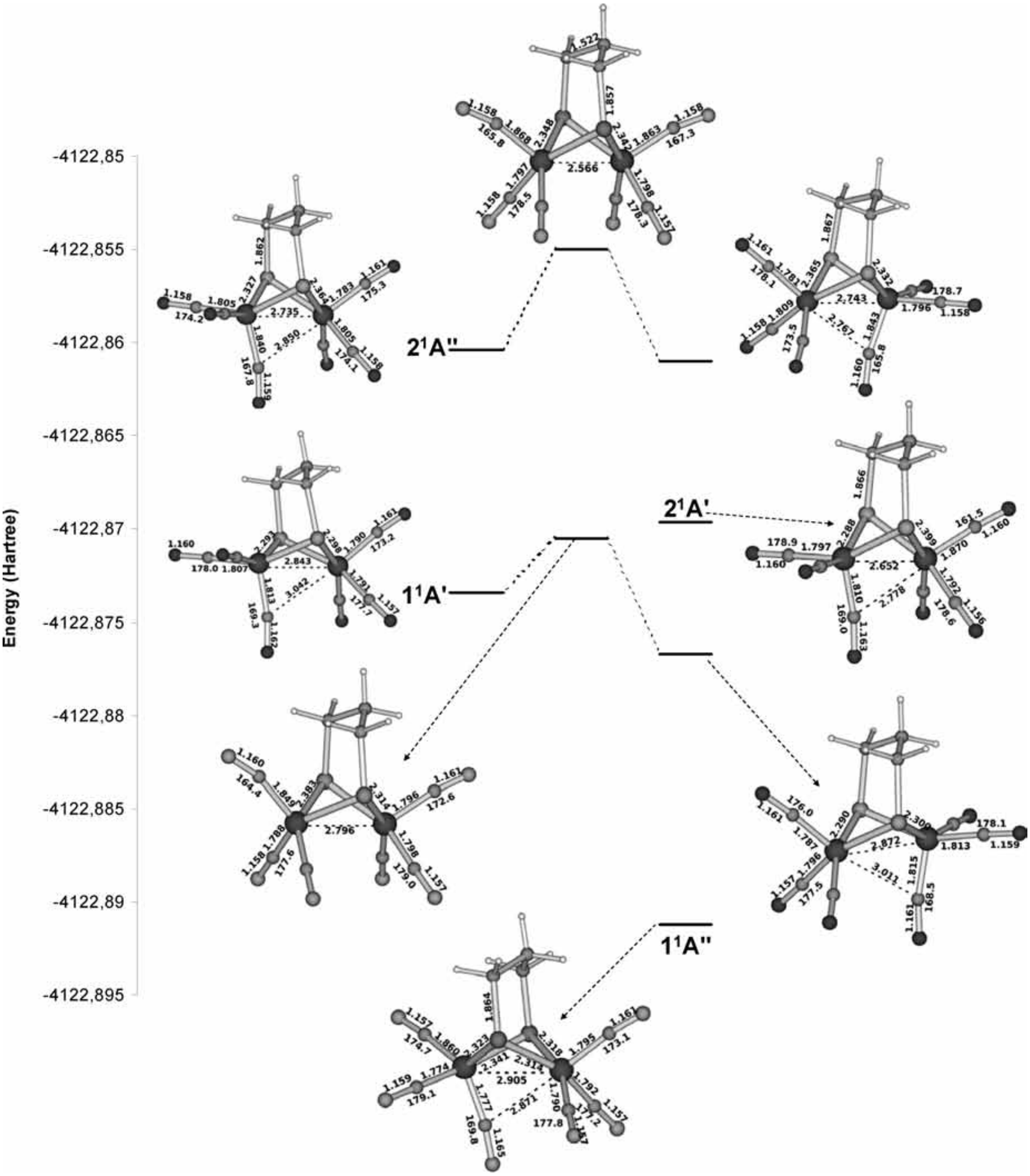

Figure 12. BP86/TZVP low-lying singlet excited-state optimized geometry parameters. Energies are given in hartree, distances are given in Å, and angles are given in degrees.

kcal·mol^{-1} B3LYP). The BP86 frontier MO energies for the singlet and triplet structures are reported in Figure 11. The HOMO and LUMO of singlet structures become the two singly occupied MOs (SOMOs) in the triplet structures. The main features of the shape of these MOs do not change significantly in going from the singlet to triplet state. In the rotated structures, the energy of the highest SOMO is significantly lowered upon the singlet−triplet excitation (0.009 and 0.01 hartree for the syn and anti isomers, respectively), while in the all-terminal CO form, the lowering is modest (0.0013 hartree). This fact can be considered one of the reasons for the stabilization of the rotated over the all-terminal CO form.

On average, all bond distances are elongated compared with those of the ground-state forms, especially at the B3LYP level; the Fe−Fe distance is increased by +0.504 (BP86) and +0.562 Å (B3LYP) as the major effect of the HOMO → LUMO triplet excitation. For the three forms considered, we found Fe−Fe RCP instead of BCP, with ρ_{rcp} values lower than the ρ_{bcp} found for the Fe−Fe ground-state bond. However, the highest ρ_{rcp} value is found for the $^3\mathbf{a}_{syn}$ global minimum (3.33×10^{-2} syn, and 3.30×10^{-2} and 2.97×10^{-2} for anti). The trend of ρ_{rcp} is in line with those previously discussed.

The fact that the triplet-state PES global minimum is rotated ($^3\mathbf{a}_{syn}$) could be relevant in the discussion of the Fe^IFe^{II} complex reduction to the Fe^IFe^I complex ($^2\mathbf{a}_{syn}^+ + e^- \rightarrow {}^1\mathbf{a}$). Following Tye et al.,[56] one can consider an Fe−Fe-based or a ligand-based reduction, according to the MO occupied by the added electron. During the initial step of the reduction, $^2\mathbf{a}_{syn}^+$ can accept one electron in its Fe-based SOMO, giving a singlet state ($^1\mathbf{a}_{syn}$), or in the LUMO, giving a triplet state ($^3\mathbf{a}_{syn}$), as found for the

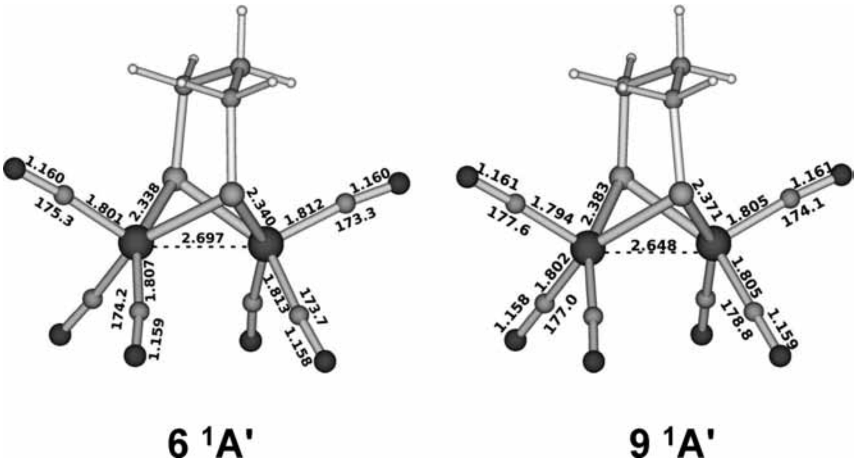

Figure 13. BP86/TZVP high-lying singlet excited-state optimized geometry parameters. Distances are given in Å, and angles are given in degree.

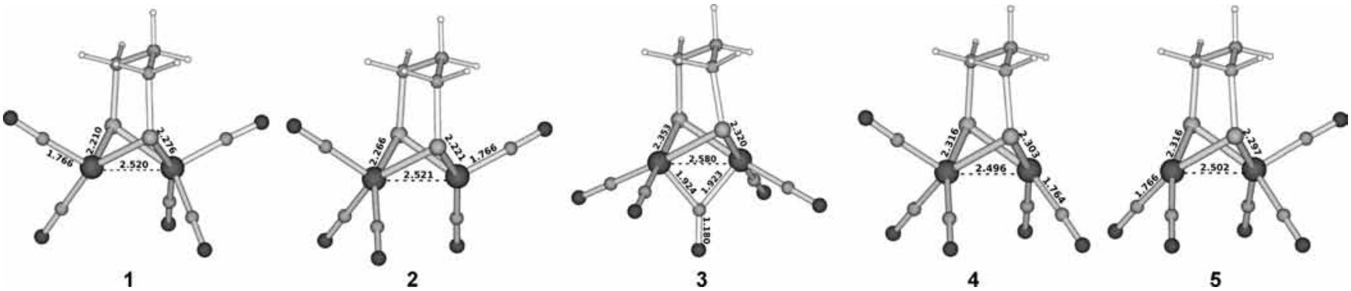

Figure 14. $Fe_2(S_2C_3H_6)(CO)_5$ BP86/TZVP-optimized geometry parameters. Distances are given in Å.

Fe^IFe^{II} (μ-pdt)$Fe_2(CO)_4(PMe_3)$(IMes) reduction. Subsequently, the structure evolves to the $^1\mathbf{a}$ product. Since both cationic and triplet-state PESs have syn rotated global minima, the initial formation of $^3\mathbf{a}_{syn}$ could occur. In order to investigate this issue, we computed the $^3\mathbf{a}_{syn}$ and $^1\mathbf{a}_{syn}$ energies at the $^2\mathbf{a}_{syn}{}^+$ geometry. We found that the singlet state is more stable than the triplet state by 26.9 kcal·mol^{-1} using BP86 and by 9.3 kcal·mol^{-1} using B3LYP, and therefore, the initial formation of a triplet state is ruled out. However, when singlet−triplet relative stability was investigated, the choice of the DFT functional was crucial, as one can see from the significant difference between BP86 and B3LYP results (17.6 kcal·mol^{-1}).

4. Discussion

4.1. Relative Stability of the All-Terminal and Rotated Forms. The issue of the stability of the rotated versus all-terminal CO forms is crucial for the design of biomimetic models of the [FeFe] hydrogenase active site.[64] This issue was already theoretically investigated by Georgakaki et al.,[42] showing the partial disruption of the bent structure of the bonding Fe−Fe HOMO and the consequent change in the Mulliken iron charges upon rotation of the $Fe(CO)_3$ units. Recently, Thomas et al.[49] analyzed the electronic structure of Fe^IFe^{II} (μ-pdt)$Fe_2(CO)_4$-(PMe_3)(IMes)$^+$. The authors found that the effect of the μ-CO ligand is the weakening of the Fe−Fe bond, with localization of the unpaired electron on the distal iron atom, in analogy with the enzyme active site.[57] Here, we contribute to this discussion in light of the results described in the previous sections.

We have shown that the rotated structures are lower in energy (i) when **a** is oxidized to $\mathbf{a}^+$ (in agreement with previous theoretical and experimental findings on Fe^IFe^{II} complexes[12,13,15,16]) and (ii) when **a** is excited to the lowest triplet or to the low-lying singly excited states. In the case of $\mathbf{a}^+$ and of the lowest triplet state, we characterized the topology of the PES on which all three forms are local minima. We found a nice correlation between the relative stability of the rotated versus all-terminal forms and Fe−Fe bond features; on a given PES (**a**, $\mathbf{a}^+$, $\mathbf{a}^-$, lowest triplet state), the most stable form is that with the highest Fe−Fe ρ_{cp} value and the lowest Fe−Fe distance. In the case of the cationic or the lowest triplet state species, this condition is realized for a rotated form, while for the neutral or anionic species, it is realized for the all terminal form. When rotated forms are considered, the formation of the Fe−C_μ interaction is substantially balanced by the weakening of the Fe−Fe bond interaction for the neutral forms, as highlighted by the decrease of δ(Fe,Fe) in going from all-terminal to rotated forms. Conversely, for the cationic all-terminal form ($^2\mathbf{a}^+$), the Fe−Fe bonding interaction is dramatically weakened (the Fe−Fe RCP instead of BCP is found) with the consequent increase of the energy, but it is restored upon $Fe(CO)_3$ group rotation (the Fe−Fe BCP is found). These results evidence the crucial role played by the strength of the Fe−Fe bonding interaction in the stability of these systems, concluding that the stabilization of the rotated forms (and therefore of the Fe−C_μ interaction) might be realized on the condition that the Fe−Fe interaction is preserved.

4.2. Singlet Excited-State Geometry Analysis. Excited-state structural distortions can be derived from the analysis of the resonance Raman (rR) spectroscopy spectra.[58] Fiedler et al.[18] obtained the rR spectra and excitation profile of the $^1\mathbf{a}$ complex, estimating the excited-state nuclear distortions from the rR intensities using the Savin formula within the time-dependent theory of Heller.[59,60] These authors found an increase of the Fe−Fe distances (0.19 and 0.30 Å) for the first and the third excited state, respectively, in agreement with the assignment of the excitation characters. Moreover, for the same two states, an increase of 0.07 and 0.09 Å for *cis*-Fe–C and of 0.05 and 0.06 Å for the *trans*-Fe–C was predicted. Finally, for both states, Fe–S increased by 0.08 Å.

We now consider the comparison between our TDDFT geometry optimization results with the predicted distortions from rR spectra.[61] It is important to recall that rR spectra investigate the excited-state Franck–Condon region, while TDDFT optimized geometries can be considered as the thermally equilibrated excited states (THEXI states), which are better investigated by time-resolved vibrational Raman measurements. Furthermore the accuracy of the bond distortions is 0.2 Å, as pointed out by Fiedler et al.[18] On average, we found only a qualitative agreement between the rR and TDDFT bond elongations for the two excited states under investigation, while absolute values can differ significantly. For example, for the first ($1^1A''$) and third ($2^1A'$) excited states, we compute Fe–Fe bond elongations of 0.363 and 0.110 Å, which differ by 0.173 and −0.190 Å with respect to the rR values. Similar considerations can be made for the other bond distances.

Two experimental studies have been recently published on **a** photoreactivity. The UV photolysis experiments by Ridley and co-workers[19] have been carried out under ambient condition in heptane using 330 nm UV pump pulses of 60 fs, and the IR spectra were collected using an IR pulse of 100 fs tuned on the wavelength of the CO ligands (2000 cm^{-1}). The time delay between the UV and IR pulse was set up to 1 ns. The experiments gave evidence of the transient formation of two (μ-pdt)$Fe_2(CO)_5$ photoproducts, obtained by removing the *cis*–*syn*- and the *trans*–*syn*-CO ligand to **a**. Furthermore, the formation of a weakly associated (μ-pdt)$Fe_2(CO)_5$–solvent adduct[62] was taken into account. The similarity of the computed CO stretching frequencies for the three candidate photoproducts with the experimental values corroborates the picture given by these authors. Similarly, Brown-McDonald and co-workers[20] studied the **a** photolysis using 365 nm light, considering samples dissolved in five different solvents. Also, these authors confirm the formation of the solvent adduct, even when noncoordinating solvent is adopted.

The TDDFT explorations of $6^1A'$ and $9^1A'$ high-lying excited-state PESs gave evidence of the stabilization of the all-terminal over the rotated forms, but a significant Fe–C anti–trans bond elongation was found for the latter. Since the estimated energy differences between rotated and all-terminal forms range between 2 and 5 kcal·mol^{-1}, the photolability of the *anti*–*trans*-CO ligand would be possible. In order to identify the photoproduct of this photochemical reaction path, we optimized the (μ-pdt)$Fe_2(CO)_5$ geometry starting from $^1\mathbf{a}_{anti}$ and $^1\mathbf{a}_{syn}$ structures, removing one anti–trans ligand. Geometry optimizations converged to the minimum structures **1** and **2**, respectively (see Figure 14).

Structure **2** was already identified by Ridley et al.[19] at the same level of theory, while structure **1** was not considered, but it was 1.5 kcal·mol^{-1} lower in energy compared to **2**. When geometry optimization was carried out starting from $^1\mathbf{a}_{anti}$ and removing the *cis*–*syn*-CO ligand, we found a local minimum (**3**), which is only 2.5 kcal·mol^{-1} higher in energy with respect to **1**. This isomer has one bridged CO, and its structure resembles the C_{2v} $Fe_2(CO)_7$ tribridged isomer.[65] However, the presence of the bridged CO (stretching mode frequency equal to 1845 cm^{-1}) does not fit with experimental IR spectra of the photoproducts, and therefore, the formation of **3** during the photolysis is ruled out. Finally, the structure already identified by Ridley et al. obtained by removing the *cis*–*syn*- (**4**) or the *cis*–*anti*-CO ligand from **a** lies 5.6 and 6.3 kcal·mol^{-1} higher in energy with respect to **1**, respectively. We conclude that **1** is the global minimum of the BP86 (μ-pdt)$Fe_2(CO)_5$ PES and one of the most probable photoproducts of **a** CO photolysis.

5. Summary and Conclusion

In this paper, we carried out an extensive DFT/TDDFT investigation of the $Fe_2(S_2C_3H_6)(CO)_6$ neutral, cationic, and anionic ground-state and low- and high-lying excited-state PESs. The results of these PES explorations have been used to discuss two important issues within the framework of the [FeFe] hydrogenase active site model's structure and photoreactivity.

We found a correlation between QTAIM electron density topology indexes and the relative stability of the rotated and all-terminal forms; on a given PES, the global minimum has the highest electron density at the Fe–Fe critical point. In the case of the cationic forms, this correlation is further corroborated by the change of signature of the Fe–Fe critical point in the all-terminal form. These facts suggest that in order to stabilize the rotated forms, one needs to shift electron density to the Fe–C_μ bond region, preserving Fe–Fe bond stability as much as possible.

We explore the first four low-lying and two high-lying singlet excited-state PESs using TDDFT. Optimized geometry parameters for the low-lying states have been compared with the geometry distortions obtained from rR analysis spectra, finding only a qualitative agreement. The explorations of two high-lying singlet excited-state PESs highlighted a significant Fe–C anti–trans bond elongation. Following the corresponding reaction path, we identified the global minimum of the $Fe_2(S_2C_3H_6)(CO)_5$ BP86 PES, which represents one probable photoproduct of the $Fe_2(S_2C_3H_6)(CO)_6$ CO photolysis.

Supporting Information Available: CASSCF analysis of the **a** forms' wave functions, FMO shape and energies, CO stretching frequencies, and the analysis of the excitation energies as a function of the DFT functional adopted. This material is available free of charge via the Internet at http://pubs.acs.org.

References and Notes

(1) Peters, W. J.; Lanzillotta, W. N.; Lemon, B. J.; Seefeld, L. C. *Science* **1998**, *282*, 1853.

(2) Pandey, A. S.; Harris, T. V.; Giles, L. J.; Peters, J. W.; Szilagyi, R. K. *J. Am. Chem. Soc.* **2008**, *130*, 4533.

(3) Nicolet, Y.; De Lacey, A. L.; Vernde, X.; Fernandez, V. M.; Hatchikian, E. C.; Fontecilla-Camps, J. C. *J. Am. Chem. Soc.* **2001**, *123*, 1596.

(4) Roseboom, W.; De Lacey, A. L.; Fernandez, V. M.; Hatchikian, E. C.; Albracht, S. P. *J. Biol. Inorg. Chem.* **2006**, *11*, 102.

(5) Chen, Z.; Lemon, B. J.; Huang, S.; Swartz, J. D.; Peters, J. W.; Bagley, K. A. *Biochemistry* **2002**, *41*, 2036.

(6) Popescu, C. V.; Munck, E. *J. Am. Chem. Soc.* **1999**, *121*, 7877.

(7) Winter, A.; Zsolnai, L.; Hutter, G. *Z. Naturforsch.* **1982**, *37b*, 1430.

(8) Lyon, E. J.; Georgakaki, I. P.; Reibenspies, J. H.; Darensbourg, M. Y. *Angew. Chem., Int. Ed.* **1999**, *38*, 3178.

(9) Borg, S. J.; Behrsing, T.; Best, S. P.; Razavet, M.; Liu, X.; Pickett, C. J. *J. Am. Chem. Soc.* **2004**, *126*, 16988.

(10) Greco, C.; Zampella, G.; Bertini, L.; Bruschi, M.; Fantucci, P.; De Gioia, L. *Inorg. Chem.* **2007**, *46*, 108.

(11) Darensbourg, M. Y.; Lyon, E. J.; Zhao, X.; Georgakaki, I. P. *Proc. Natl. Acad. Sci. U.S.A.* **2003**, *100*, 3683.

(12) Liu, T.; Darensbourg, M. Y. *J. Am. Chem. Soc.* **2007**, *129*, 7008.

(13) Justice, A. K.; Rauchfuss, T. B.; Wilson, S. R. *Angew. Chem., Int. Ed.* **2007**, *46*, 6152.

(14) Justice, A. K.; Zampella, G.; De Gioia, L.; Rauchfuss, T. B. *Chem. Commun.* **2007**, 2019.

(15) Felton, G. A. N.; Vannucci, A. K.; Chen, J.; Lockett, L. T.; Okumura, N.; Petro, B. J.; Zakai, U. I.; Evans, D. H.; Glass, R. S.; Lichtenberger, D. L. *J. Am. Chem. Soc.* **2007**, *129*, 12521.

(16) Cheah, M. H.; Tard, C.; Borg, S. J.; Liu, X.; Ibrahim, S. K.; Pickett, C. J.; Best, S. P. *J. Am. Chem. Soc.* **2007**, *129*, 11085.

(17) Bertini, L.; Bruschi, M.; De Gioia, L.; Fantucci, P.; Greco, C.; Zampella, G. *Top. Curr. Chem.* **2007**, *268*, 1.

(18) Fiedler, A. T.; Brunold, T. C. *Inorg. Chem.* **2005**, *44*, 1794.

(19) Ridley, A. R.; Stewart, A. I.; Adamczyk, K.; Ghosh, H. N.; Kerkeni, B.; Guo, Z. X.; Nibbering, E. T. J.; Pickett, C. J.; Hunt, N. T. *Inorg. Chem.* **2008**, *47*, 7453.

(20) Brown-McDonald, J.; Berg, S.; Peralto, M.; Works, C. *Inorg. Chim. Acta* **2009**, *362*, 318.

(21) Becke, A. D. *Phys. Rev. A* **1988**, *38*, 3098.

(22) Perdew, J. P. *Phys. Rev. B* **1986**, *33*, 8822.

(23) Lee, C.; Yang, W.; Parr, R. G. *Phys. Rev. B* **1988**, *37*, 785.

(24) Vosko, S.; Wilk, L.; Nussair, M. *Can. J. Phys.* **1980**, *58*, 1200.

(25) Eichkorn, K.; Weigend, F.; Treutler, O.; Ahlrichs, R. *Theor. Chem. Acc.* **1997**, *97*, 119.

(26) Schafer, A.; Huber, C.; Ahlrichs, R. *J. Chem. Phys.* **1994**, *100*, 5829.

(27) Furche, F.; Ahlrichs, R. *J. Chem. Phys.* **2002**, *117*, 7433.

(28) Ahlrichs, R.; Bar, M.; Haser, M.; Horn, H.; Kolmel, C. *Chem. Phys. Lett.* **1989**, *62*, 165.

(29) Rappoport, D.; Furche, F. *J. Chem. Phys.* **2005**, *122*, 064105.

(30) Bertini, L.; Greco, C.; De Gioia, L.; Fantucci, P. *J. Phys. Chem. A* **2006**, *110*, 12900.

(31) Beigler-Konig, F. W.; Bader, R. W. F.; Tang, H.-T. *J. Comput. Chem.* **1982**, *317*, 3.

(32) Gatti C. *CNR-ISTM*; University of Milan: Milano, Italy, 2007.

(33) Gatti, C.; Lasi, D. *Faraday Discuss.* **2007**, *135*, 55.

(34) Macchi, P.; Sironi, A. *Coord. Chem. Rev.* **2003**, *283*−*239*, 383.

(35) Reinhold, J.; Kluge, O.; Mealli, C. *Inorg. Chem.* **2007**, *46*, 7142.

(36) Platts, J. A.; Evans, G. J. S.; Coogan, M. P.; Overgaard, J. *Inorg. Chem.* **2007**, *46*, 6291.

(37) Teo, B. K.; Hall, M. B.; Fenske, R. F.; Dahl, L. F. *Inorg. Chem.* **1975**, *14*, 3103.

(38) DeKock, L. R.; Baerends, E. J.; Oskam, A. *Inorg. Chem.* **1983**, *22*, 4158.

(39) DeKock, L. R.; Baerends, Hengelmolen, R. *Organometallics* **1984**, *3*, 289.

(40) Tye, J. W.; Darensbourg, M. Y.; Hall, M. B. *J. Comput. Chem.* **2006**, *27*, 1454.

(41) Lyon, E. J.; Georgakaki, I. P.; Reibenspies, J. H.; Darensbourg, M. Y. *J. Am. Chem. Soc.* **2001**, *123*, 3268.

(42) Georgakaki, I. P.; Thomson, L. M.; Lyon, E. J.; Hall, M. B.; Darensbourg, M. Y. *Coord. Chem. Rev.* **2003**, *238*−*239*, 255.

(43) Roy, E. L.; Batista, E. R.; Hay, P. J. *Inorg. Chem.* **2008**, *47*, 9229.

(44) Petro, B. J.; Vannucci, A. K.; Lockett, L. T.; Mebi, C.; Kottani, R.; Gruhn, N. E.; Gary, S.; Nichol, G. S.; Goodyer, P. A. J.; Evans, D. H.; Richard, S.; Glass, R. S.; Lichtenberger, D. L. *J. Mol. Struct.* **2008**, *890*, 281.

(45) The **a** reorganization energy is defined as the difference between the energy of **a** at its minimum geometry and that at the $\mathbf{a}^+$ minimum geometry.

(46) Adamo, C.; Scuseria, G.; Barone, V. *J. Chem. Phys.* **1999**, *111*, 2889.

(47) Adamo, C.; Barone, V. *Theor. Chem. Acc.* **2000**, *105*, 169.

(48) Vlêck, A., Jr.; Zaliŝ, S. *Coord. Chem. Rev.* **2007**, *258*, 258.

(49) Thomas, C. M.; Darensbourg, M. Y.; Hall, M. B. *J. Inorg. Biochem.* **2007**, *101*, 1752.

(50) Borg, S. J.; Tye, J. W.; Hall, M. B.; Best, S. P. *Inorg. Chem.* **2007**, *46*, 384.

(51) A critical point (CP) is a stationary point of the electron density characterized by the rank (the sum of the non-zero hessian eigenvalues) and the signature (the sum of the sign of the element of the diagonalized hessian). A bond critical point (BCP) denotes a (3,−1) first-order saddle point of electron density along the maximum electron density line between two atoms. A (3,+1) ring critical point (RCP) is a second-order saddle point in the electron density, which often identifies rings in molecules.

(52) Bader, R. F. W. *Atoms in Molecules. A Quantum Theory*; Cambridge University Press: Oxford, U.K., 1991.

(53) Corts-Guzmna, F.; Bader, R. F. W. *Coord. Chem. Rev.* **2005**, *249*, 633.

(54) On the $^1A''$ PES computed using DFT and imposing C_s symmetry, the three forms of the system are transition states, with the anti rotated structure as the lowest in energy with respect to the syn rotated and the all-terminal structures (+3.3 and +4.4 kcal·mol^{-1} higher in energy with respect to the anti structure, respectively).

(55) Bertini, L.; Bruschi, M.; De Gioia, L.; Fantucci, P. *J. Phys. Chem. A* **2007**, *111*, 12152.

(56) Tye, J. W.; Lee, J.; Wang, H.-W.; Mejia-Rodriguez, R.; Reibenspies, J. H.; Hall, M. B.; Darensbourg, M. Y. *Inorg. Chem.* **2005**, *44*, 5550.

(57) Thomas, C. M.; Liu, T.; Hall, M. B.; Darensbourg, M. Y. *Inorg. Chem.* **2008**, *47*, 7009.

(58) Zink, J. I. *Coord. Chem. Rev.* **2001**, *211*, 69.

(59) Warshel, A.; Dauber, P. *J. Chem. Phys.* **1977**, *66*, 5477.

(60) Heller, E. J. *Acc. Chem. Res.* **1981**, *14*, 368.

(61) Mroginski, M.-A.; Kneip, C.; Hildebrand, P.; Mark, F. *J. Mol. Struct.* **2003**, *661*−*662*, 611.

(62) Moskovich, S.; Reuvenov, D.; Schultz, R. H. *Chem. Phys. Lett.* **2006**, *431*, 62.

(63) The lowest-energy structure found during the all-terminal structure optimization (7.2 kcal·mol^{-1} higher in energy with respect to the anti structure; gradient norm vector 0.04 hartree·Å^{-1}) has an Fe−Fe bond distance of 2.730 Å.

(64) Tye, J. W.; Darensbourg, M. Y.; Hall, M. B. *Inorg. Chem.* **2006**, *45*, 1552.

(65) Xie, Y.; Schaefer, F.; King, R. B. *J. Am. Chem. Soc.* **2000**, *122*, 8746.

JP809347H